PNAS RESEARCH ARTICLE | CELL BIOLOGY

ATP8B1 regulates PIP2 localization and cleavage of pyroptotic executioner Gasdermin D

Nilam Bhandari[a,b,1], Ashutosh Prince[a,b,1], Mariam R. Khan[a,b], C. Alicia Traughber[a,b], Kalash Neupane[a,b], Shuhui W. Lorkowski[c], Gregory Brubaker[c], Elif G. Ertugral[d], Chandrasekhar R. Kothapalli[d], George R. Dubyak[e], Jonathan D. Smith[c], and Kailash Gulshan[a,b,c,2]

Affiliations are included on p. 11.

Edited by David Russell, University of Texas Southwestern Medical Center, Dallas, TX; received March 19, 2025; accepted April 22, 2025

Mutations in *ATP8B1* cause progressive familial intrahepatic cholestasis, with symptoms including pruritus, pancreatitis, fat malabsorption, intestinal inflammation, and failure to thrive. High-throughput studies showed interconnection between ATP8B1 and phosphoinositide (PIPs), but the mechanism linking ATP8B1, lipid metabolism, and inflammation remains unclear. *Atp8b1*$^{G308V/G308V}$ mouse model, unbiased RNAseq, high-resolution-stimulation emission depltion (STED)-microscopy, and Crispr-Cas9 generated *ATP8B1*$^{-/-}$ knockouts in hepatocytes/monocytes/macrophages were used to determine role of ATP8B1 in phosphatidylinositol,4-5-bisphosphate (PIP2) trafficking and inflammation. Human ATP8B1, purified from Sf9 insect cells and reconstituted in proteoliposomes, was used to test cell-free PIP2 flip. Various in-vitro techniques were used for testing direct interaction between PIP2 and ATP8B1. ATP8B1 maintains PIP2 at the inner leaflet of plasma membrane (PM). ATP8B1 flips PIP2 in cells, without altering flip of PE or bulk-endocytosis. ATP8b1 flips PIP2 in a cell-free system. ATP8B1 deletion promotes bile-salt-mediated cholesterol extraction from hepatocytes in a PIP2-dependent manner. PIP2 directly binds to the P-loop of ATP8B1. Unbiased RNAseq showed upregulation of inflammatory cytokines in ATP8b1$^{-/-}$ immune cells. *ATP8B1*$^{-/-}$ monocytes/macrophages showed aberrant lipopolysaccharide (LPS)-induced cleavage of GSDMD, formation of GSDMD pores, and interleukin-1beta (IL1β) release. Inflammation-resolving efferocytosis was impaired in *ATP8B1*$^{-/-}$ macrophages. Biophysical properties of PM were altered in *ATP8b1*$^{-/-}$ cells, with the mechanism being disrupted localization of PIP2. *Atp8b1*$^{G308V/G308V}$ mice exposed to LPS showed higher plasma IL1β and lower survival rates vs. WT mice. ATP8B1 maintains PIP2 at the inner leaflet of PM. ATP8b1 directly flips and binds PIP2. ATP8B1 regulates LPS-induced GsdmD cleavage, formation of GsdmD pores, IL1β release, and mortality in mice.

PFIC1 | Gasdermin D | inflammasome | PIP2 | ATP8b1

Significance

Depletion of signaling lipid phosphatidylinositol,4-5-bisphosphate (PIP2) from the inner leaflet of plasma membrane (PM) is linked to heart failure, Alzheimer's, cancer, and other diseases. We show that ATP8B1 maintains PIP2 at the inner leaflet of PM and serves as the PIP2 flippase. ATP8B1 deficiency or ATP8B1-mutations can increase the risk of disease induced by PIP2 mislocalization. progressive familial intrahepatic cholestasis (PFIC1) patients show extrahepatic inflammation, but the mechanism is unclear. We describe a role of ATP8B1 in activation of highly inflammatory pyroptotic executor Gasdermin D. Humans are always exposed to small doses of lipopolysaccharide (LPS) (from gut bacteria), and this low-dose LPS exposure may fuel inflammation in immune cells of PFIC1 patients.

Human mutations in ATP8B1 cause progressive familial intrahepatic cholestasis 1 (PFIC1), leading to liver failure and extrahepatic manifestations (1, 2). The phenotypic spectrum of ATP8B1 deficiency in humans ranges from severe to moderate/mild, but the mechanism(s) regulating pleiotropic effects of ATP8B1 mutations on lipid homeostasis and inflammation is unclear.

Minor signaling lipid phosphatidylinositol 4,5-bisphosphate (PIP2) regulates several cellular processes (3, 4). Cellular PIP2 levels are dynamic and reflect the net contribution of lipid kinases and phosphatases, but the distinct feature that allows PIP2 to execute various functions is its almost exclusive enrichment at the inner leaflet of the PM. Despite the wide variety of physiological functions of PIP2, it is still unclear how PIP2 remains restricted at the inner leaflet of the PM. We previously identified ABCA1, a cholesterol/lipid efflux pump, as the first known PIP2 floppase from any system (5). PIP2 floppase activity of ABCA1 was also confirmed in other model systems (6, 7). PIP2 flip, on the other hand, has not yet been described, and the identity of PIP2 flippase remains unknown.

ATP8B1 belongs to the P4 type ATPases family, a family of proteins involved in a variety of human diseases, with the main function being the translocation of phospholipids across PM bilayer (8, 9). Mutations in ATP8B1 lead to a compromised detergent-resistant state of the hepatic canalicular membrane (10, 11). The loss of cholesterol from the canalicular membrane in PFIC1 is proposed to negatively regulate the activity of the bile salt exporter pump, leading to increased cholestasis (12). While much is known about the pathophysiology of PFIC1, the underlying mechanism remains unclear. The phosphatidylserine (PS) flippase activity of ATP8B1 was proposed to be involved in maintaining the integrity of the hepatic canalicular membrane (13), while another study proposed a

Author contributions: K.G. designed research; N.B., A.P., M.R.K., C.A.T., K.N., S.W.L., G.B., E.G.E., and K.G. performed research; K.G. contributed new reagents/analytic tools; C.R.K., G.R.D., J.D.S., and K.G. analyzed data; and N.B., A.P., M.R.K., and K.G. wrote the paper.

The authors declare no competing interest.

This article is a PNAS Direct Submission.

Copyright © 2025 the Author(s). Published by PNAS. This article is distributed under Creative Commons Attribution-NonCommercial-NoDerivatives License 4.0 (CC BY-NC-ND).

[1]N.B. and A.P. contributed equally to this work.

[2]To whom correspondence may be addressed. Email: k.gulshan@csuohio.edu.

This article contains supporting information online at https://www.pnas.org/lookup/suppl/doi:10.1073/pnas.2502798122/-/DCSupplemental.

Published May 29, 2025.

flippase-independent function of ATP8B1 in the formation of microvilli structures (14). Mutations in the ATP8B1 gene cause hearing loss in humans/mice, associated with progressive degeneration of cochlear hair cells (15). Similar to ATP8B1, PIP2 is also critical for mechanical transduction and adaptation of hair cells (16, 17). Interestingly, a high-throughput proteomic analysis proposed that ATP8B1 flippase activity and phosphoinositide metabolism may be interconnected at the Golgi (18), and more recently, ATP8B1 was shown to be regulated by phosphoinositides (19), but the mechanistic link between ATP8B1 and phosphatidylinositol phosphates (PIPs) metabolism is still not clear.

PFIC1 patients often show clinical features such as fat malabsorption, largely due to the lack of bile acids in the intestine, while diarrhea, and pancreatitis tend to be more common post liver transplantation (20). *ATP8B1* deficiency in human peripheral blood monocyte-derived macrophages (HMDMs) was shown to result in incomplete polarization of HMDMs into M2c (21), but the contribution/mechanism of inflammasome and inflammation-resolving pathways in PFIC1 is not clear. Pyroptosis executor GSDMD, a membrane pore-forming protein, promotes a variety of inflammatory diseases (22–25). Pyroptosis can be induced by canonical or noncanonical inflammasome pathways. Canonical inflammasome-mediated cleavage of GSDMD in macrophages occurs via caspase-1, and in a two-step process with priming by molecules such as lipopolysaccharide (LPS) or ox-LDL, and activation by secondary damage signal (extracellular adenosine triphosphate (ATP), lysosomal damage, or ionophores). The noncanonical inflammasome is induced upon sensing of cytosolic LPS from gram-negative bacteria, leading to GSDMD cleavage by the related caspase-4/5 (caspase-11 in mice). GSDMD cleavage and release of GSDMD N-terminal fragment via a noncanonical inflammasome pathway can in turn, activate the NLRP3 canonical inflammasome in a positive feedback loop (26). GSDMD is thus a common executor of both canonical and noncanonical inflammasome activity. The role and mechanism of the GSDMD and inflammasome pathway in PFIC1 are not yet described.

Results

ATP8B1 Restricts PIP2 at the Inner Leaflet of the PM. Crispr-Cas9 generated homozygous *ATP8B1* knockouts (*ATP8B1*$^{-/-}$) were constructed in various cell lines with deletions confirmed by qRT-PCR and sequencing (*SI Appendix*, Fig. S1), and all data were confirmed in two independent Crisrp-Cas9 deletion clones. Using an established flow cytometry-based PIP2 antibody binding assay (5), a ~twofold increase in PIP2 exposure at the cell surface was observed in the *ATP8B1*$^{-/-}$ macrophages (Fig. 1*A*). ABCA1 expression can increase cell-surface exposure of PIP2 (5, 6). An additive effect was observed in the *ATP8B1*$^{-/-}$ cells expressing ABCA1, with a ~3.6-fold increase in PIP2 exposure vs. control cells (Fig. 1 *A* and *B*). To test the specificity, cells were pretreated with PIP2 or PI3P blocking proteins, and as shown in Fig. 1*A*, blocking PIP2 but not PI3P reduced PIP2 antibody binding to the basal level. Control IgM-FITC binding was not altered in WT vs. *ATP8B1*$^{-/-}$ cells (*SI Appendix*, Fig. S2*A*). Furthermore, the HepG2 *ATP8B1*$^{-/-}$ cells also showed more PIP2 exposure, assessed via fluorescent spectroscopy (Fig. 1*C*) and confocal laser scanning microscopy (Fig. 1*D* and *SI Appendix*, Fig. S2*B*). These data were also confirmed in RAW264.7-Atp8b1$^{-/-}$ macrophages (*SI Appendix*,

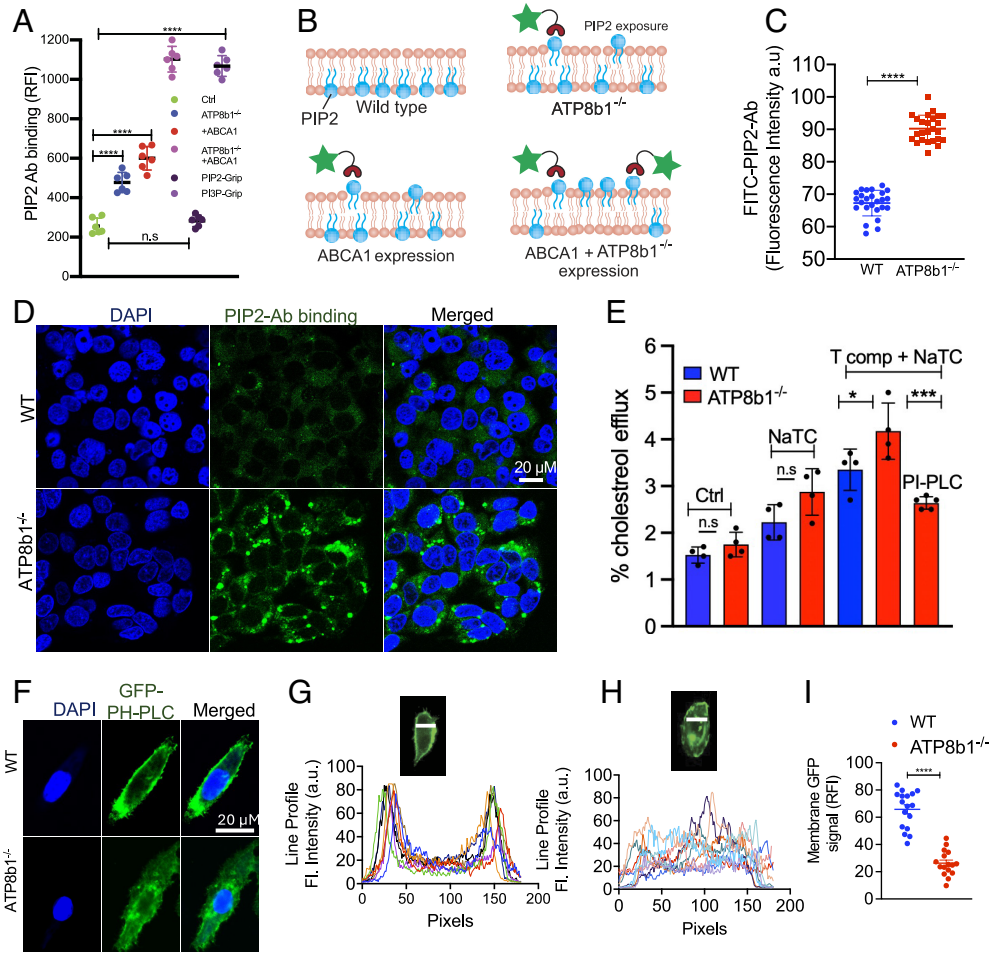

Fig. 1. ATP8B1 restricts PIP2 at the plasma membrane in vitro and in vivo. (*A*) Cell surface PIP2 determined by flow cytometry using FITC-PIP2 antibody,±ABCA1±PIP2 Grip, or±PI3P Grip (RFI, relative fluorescence intensity; n = 6, mean ± SD; ****show $P < 0.0001$, n.s = nonsignificant by ANOVA posttest). (*B*) Model depicting PIP2 exposure and FITC-PIP2 antibody binding at the exoplasmic side of the PM bilayer. (*C*) Fluorescent spectroscopic quantification of binding of FITC-PIP2 antibody to WT or ATP8B1$^{-/-}$ HePG2 cells (25 independent wells were read/sample, values are mean ± SD; **** show $P < 0.0001$ by the *t* test). (*D*) Confocal microscopy of nonpermeabilized WT or *ATP8B1*$^{-/-}$ HePG2 cells probed with FITC-PIP2 antibody. (*E*) Bile-salt induced cholesterol extraction from WT or *ATP8B1*$^{-/-}$ HePG2 cells ± ABCA1 expression or ±PI-PLC treatment (N = 3, values are mean ± SD, n.s, nonsignificant, *$P < 0.05$, ***$P < 0.001$, by ANOVA posttest). (*F*) Confocal microscopy of HepG2 cells (WT or *ATP8B1*$^{-/-}$) stably transfected with PIP2 reporter (2X-PH-PLC-eGFP). (*G*) Cell scan profile showing the fluorescent intensity of PIP2 reporter at the PM and cytoplasmic region of WT or (*H*) *ATP8B1*$^{-/-}$ HePG2 cells. (*I*) Quantification of % fluorescence intensity of PIP2-GFP reporter at the PM, values are mean ± SD; **** show $P < 0.0001$ by the *t* test.

Fig. S2*C*). To determine the physiological consequences of PIP2 exposure in *ATP8B1*$^{-/-}$ cells, bile-salt-mediated cholesterol extraction was measured. As shown in Fig. 1*E*, bile salts extracted significantly more cholesterol from the *ATP8B1*$^{-/-}$ hepatocytes, while excision of exposed PIP2 by phosphatidylinositol-specific phospholipase (PI-PLC) alleviated this effect. These data indicated that cell-surface PIP2 in *ATP8B1*$^{-/-}$ cells promotes excessive cholesterol extraction by bile salts.

To determine whether there is a concomitant reduction in PIP2 levels at the cytoplasmic side of the PM bilayer, WT or *ATP8B1*$^{-/-}$ -HepG2 cells were stably transfected with a fluorescent PIP2 binding reporter construct (2X-PH-PLC-eGFP). As expected, the PIP2 reporter decorated the inner leaflet of the PM in the WT cells, while in *ATP8B1*$^{-/-}$ cells, the PIP2 reporter was redistributed from PM to the cytoplasm. (Fig. 1*F*). The fluorescent intensity scan of WT cells showed two distinct fluorescent peaks originating from the two flanks of PM (Fig. 1*G*), while the *ATP8B1*$^{-/-}$ cells showed a fluorescent peak originating from the cytoplasmic region (Fig. 1*H*). Quantification of the GFP signal showed that ~65% PIP2 is localized at the PM in WT cells (Fig. 1*I*). In contrast, *ATP8B1*$^{-/-}$ cells showed only ~27% PIP2 at the PM (Fig. 1*I*).

ATP8B1 Is a PIP2 Flippase. To determine whether ATP8B1 is involved in PIP2 flip, a time-lapse microscopy-based assay using fatty acid-labeled Bodipy-TMR-PIP2 was employed (Fig. 2*A*). The WT HepG2 cells showed flip of exogenous PIP2 allowing it to accumulate at the PM over time, with PIP2 signal on the PM appearing in ~3 to 5 min (Fig. 2*B*, *SI Appendix*, Fig. S3*A*, and Movies S1 and S2), while the *ATP8B1*$^{-/-}$ cells showed marked reduction in PIP2 accumulation at PM, presumably due to PIP2 exchanging back to the media from the outer leaflet of the PM bilayer (Fig. 2*B*, *SI Appendix*, Fig. S3*B*, and Movies S3 and S4). Quantification of the Bodipy-PIP2 signal at the PM over time showed defective PIP2 flip in *ATP8B1*$^{-/-}$ cells (Fig. 2*C*). The RAW264.7 macrophages showed a much faster rate of PIP2 flip with a strong Bodipy-PIP2 signal at the PM within ~30 to 90 s (Fig. 2*D*, *SI Appendix*, Fig. S4*A*, and Movies S5 and S6), indicating that kinetics of PIP2 flip may be cell-type dependent. In contrast, the RAW264.7-*Atp8b1*$^{-/-}$ macrophages showed markedly reduced PIP2 flip (Fig. 2*D*, *SI Appendix*, Fig. S4*B*, and Movies S7 and S8). Quantification of time-dependent PIP2 incorporation in the PM showed markedly defective PIP2 flip in RAW264.7- *Atp8b1*$^{-/-}$ cells (Fig. 2*E*). The flip of phosphatidylethanolamine (PE) was unaffected in *Atp8b1*$^{-/-}$ cells (Fig. 2 *F* and *G*, *SI Appendix*, Fig. S5*A*, and Movies S9–S12), indicating the specificity of ATP8B1 toward flipping PIP2. Furthermore, no differences were found in bulk-endocytosis in WT vs. *ATP8B1*$^{-/-}$ cells, with no changes in binding or endocytosis of FM1-43 dye (*SI Appendix*, Fig. S5 *B* and *C*).

To further test the role of flippase in PIP2 translocation inside the cells, rather than endocytosis, a recently reported confocal-microscopy-based phospholipid flip assay was used (27). As shown in Fig. 2*H*, WT-HePG2 cells showed an intense fluorescent signal inside the cell after BSA wash, indicating robust PIP2 flip. In contrast, *ATP8B1*$^{-/-}$ cells showed a weak signal at the PM in the form of puncta after BSA wash (Fig. 2*H*), reminiscent of endocytosis rather than ATPase-mediated active PIP2 flip. The flip of PE was unaffected in *ATP8B1*$^{-/-}$ cells (Fig. 2*I*). The quantification of flipped NBD-PIP2 showed ~fourfold reduction in HepG2-*ATP8B1*$^{-/-}$ vs. WT cells (Fig. 2*J*), while no differences were found in the flip of NBD-PE (Fig. 2*K*).

ATP8B1 deletion may affect PIP2 translocation due to changes in membrane properties or by indirectly influencing the activity of other proteins involved in lipid trafficking. To determine whether ATP8B1 can directly flip PIP2, a cell-free system was reconstituted. The GST-tagged human ATP8B1 protein was cloned in a baculovirus, followed by transduction of insect Sf9 cells, and expression was confirmed by western blot using anti-GST antibody (*SI Appendix*, Fig. S6). The ATPase activity of full-length ATP8B1 was determined in the presence of various phospholipids, and a notable increase in ATPase activity was observed with 300 μM PIP2 (Fig. 2*L*). The EC_{50} values of PIP2 and PS-stimulated activity of ATP8B1 were 231.5 ± 35.2 μM and 283 ± 33.3 μM, respectively (Fig. 2*M*). The EC_{50} values of PC-stimulated activity of ATP8B1 was 1.75-fold higher than PIP2 (Fig. 2*M*).

Next, we utilized reconstituted ATP8B1-proteoliposomes with NBD-labeled phospholipids and sodium dithionite quenching assay to measure phospholipid flip (Fig. 2*N*), as described before (28–30). A marked decrease in the fluorescence intensity of NBD-PIP2 was observed following dithionite quenching of ATP8B1 containing proteoliposomes vs. control liposomes, with ~12% NBD-PIP2 flip in 5 min, ~22% NBD-PIP2 flip in 30 min, and ~27% NBD-PIP2 flipped in 60 min (Fig. 2 *O* and *P*). No significant changes were observed in the flip of NBD-PE, indicating that ATP8B1 does not play a direct role in the flip of PE (Fig. 2 *Q* and *R*).

PIP2 Directly Binds ATP8B1. Several PIP2 binding proteins contain a noncanonical signature motif KXXXXXXXXK/RXR, allowing binding to PIP2 (9, 31). Using computational analysis, a conserved and putative PIP2 binding motif KFPRTEEERRMR, from amino acids 824-835 in the P2 domain of the P-loop region of ATP8B1 was identified (Fig. 3 *A* and *B*). PONDER prediction (*SI Appendix*, Fig. S7*A*), helical wheel diagram (*SI Appendix*, Fig. S7*B*), and Alpha-fold prediction analysis indicated that the PIP2 binding region of ATP8B1 is disordered and forms a putative binding surface for anionic moieties (*SI Appendix*, Fig. S7*C*). To determine the direct binding between ATP8B1 and PIP2, recombinant fragments of WT or PIP2-binding-domain (PBD) mutant isoform of ATP8B1 (77 amino acid residues from 803 to 880) were purified. The mutated isoform contained alanine substitutions of conserved amino acid residues K824A, R832A, R833A, and R835A. The purity and sequences of protein fragments were confirmed by reverse phase chromatography and Mass-Spec (LC–MS) analysis (*SI Appendix*, Fig. S8). The binding between ATP8B1 and PIP2 was determined using Surface Plasmon Resonance (SPR), as described earlier (5). The WT or PBD mutant isoforms of ATP8B1 were immobilized by covalent coupling on a CM5 sensor chip using EDC-NHS reagent, followed by injection of different concentrations of PIP2. As shown in Fig. 3*C*, WT ATP8B1 showed robust binding with PIP2 with K_d of ~11.5 μM, while the PBD mutant of ATP8B1 showed weak binding with K_d of ~63.6 μM (Fig. 3*D*). Microscale thermophoresis (MST) analysis also showed a dose-dependent alteration in the mobility of WT ATP8B1 protein on the surface of PIP2 containing liposomes (Fig. 3*E*), indicating binding between ATP8B1 and PIP2, while PBD mutant of ATP8B1 showed markedly weak interaction (Fig. 3*F*). The K_d of WT ATP8B1 was ~3.74 ± 0.61 μM, vs. K_d of ~29.7 ± 0.57 μM for PBD mutant protein (Fig. 3*G*). To determine whether ATP8B1 and PIP2 can interact in proximity (<10 nm), a spectroscopy-based fluorescence resonance energy transfer (FRET) assay was performed, as described earlier (32). Alexa-488 labeled ATP8B1 protein fragments and Rhodamine PE doped Large Unilamellar Vesicles (LUVs) (1,2-Dioleoyl-sn-glycero-3-phosphocholine (DOPC) ± 5 mol% PIP2) pairs were used for FRET. A clear interaction was observed between ATP8B1 and PIP2 (Fig. 3*H*), while the PBD mutant of ATP8B1 showed much lower FRET efficiency (Fig. 3*I*). Next, to determine the interaction between PIP2 and ATP8B1 in a micrometer scale and membrane environment, confocal microscopy using giant unilamellar vesicles

(GUVs) was performed. As shown in Fig. 3*J*, a strong binding of ATP8B1 was observed on the membrane surface of PIP2-containing GUVs, with a homogenous distribution of Alexa488-WT-ATP8B1 (green fluorescence) on equatorial section of GUVs (red fluorescence). The PBD mutant isoform of ATP8B1 showed markedly reduced binding with PIP2-containing GUVs (Fig. 3*J*). Quantification of the oval profile of Alexa488 fluorescence revealed significantly higher binding of ATP8B1 with PIP2 vs. PBD-mutant form of ATP8B1 (Fig. 3*K*).

Unbiased RNAseq of ATP8B1$^{-/-}$ Cells Reveals Alterations in Inflammatory Pathways. To determine the effect of *ATP8B1* deletion on genome-wide transcriptional profile, the *ATP8B1*$^{-/-}$-HepG2 cells, *ATP8B1*$^{-/-}$-THP-1 macrophages, and *ATP8B1*$^{-/-}$-THP-1 monocytes were subjected to an unbiased RNAseq analysis vs. WT controls. The top altered pathways in ATP8B1$^{-/-}$ hepatocytes included signal transduction, cell adhesion, microvillus assembly, phospholipid translocation, and bile acid metabolism (*SI Appendix*, Fig. S9*A*). As shown in Fig. 4 *A* and *B*, the altered genes included MASP1, which

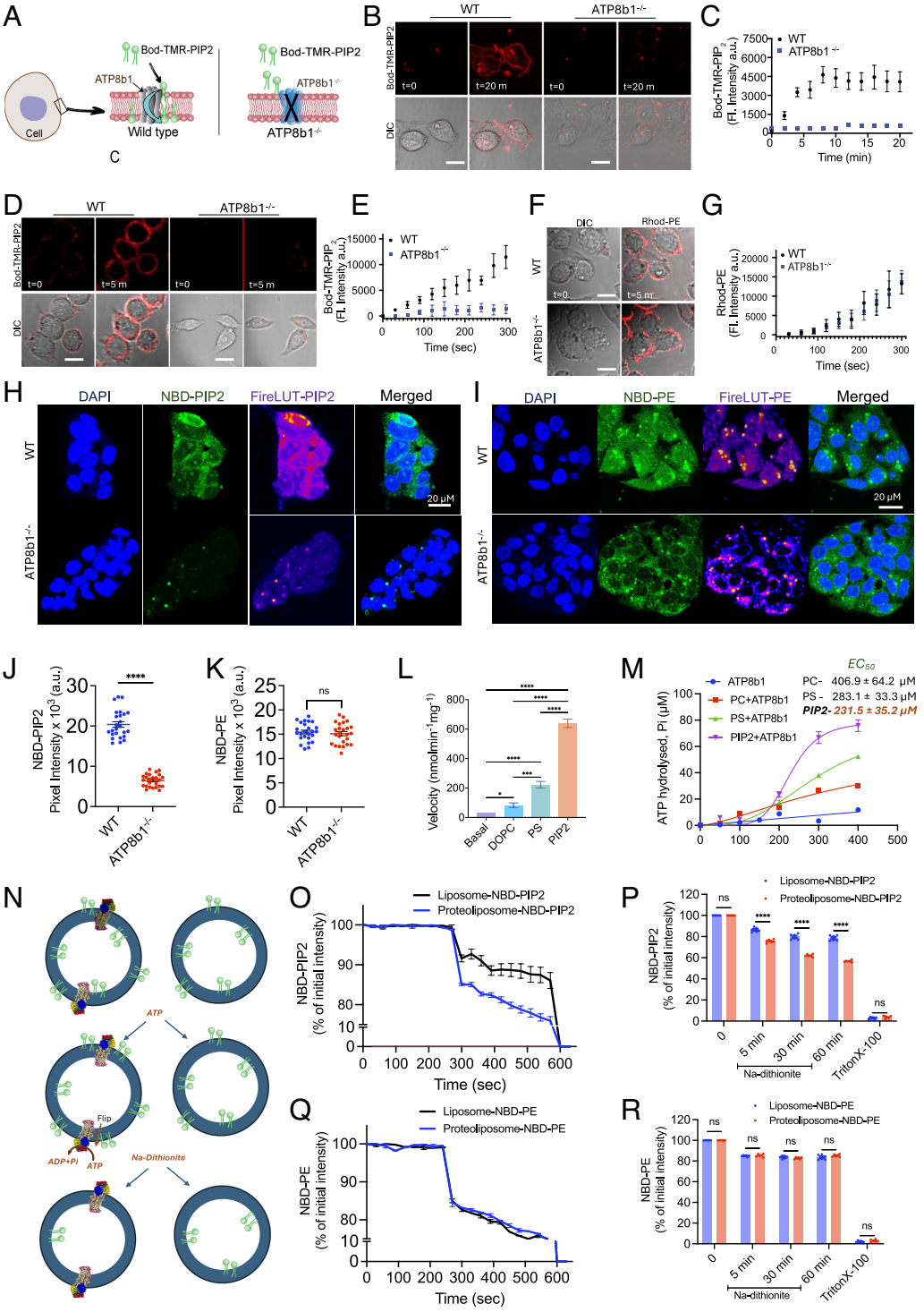

Fig. 2. ATP8B1 is a PIP2 flippase. (*A*) Schematic diagram showing the experimental design for PIP2 flip assay. (*B*) Live cell imaging showing flip of exogenous Bodipy-TMR-PIP2 into the PM of HepG2-WT cells or HepG2-*ATP8B1*$^{-/-}$ cells over time. (*C*) Graph showing the fluorescence intensity of Bodipy-TMR-PIP2 over time. Values are mean intensity ± SE. (*D*) Bodipy-TMR-PIP2 flip into the PM of RAW264.7-WT or *Atp8b1*$^{-/-}$ cells over time. (*E*) Fluorescence intensity of Bodipy-TMR-PIP2 over time. Values are mean intensity ± SE. (*F*) Live cell imaging of RAW264.7-WT and *Atp8b1*$^{-/-}$ cells showing flip of Rhodamine PE over time. (*G*) Fluorescence intensity profile of Rhodamine PE over time. Values are mean intensity ± SE. The scale bar for all micrographs is 5 µm. (*H* and *I*) WT or *ATP8b1*$^{-/-}$ HepG2 cells preincubated with phospholipase inhibitors at 20 °C were supplemented with NBD-PIP2, or NBD-PE, followed by incubation for up to 60 min to allow lipid internalization. Cells were subjected to backexchange with BSA, followed by TBSS wash, and visualization by confocal laser scanning microscopy. FIRE look-up table (ImageJ) was used to highlight intensity variations in PIP2 flip. Images are representative of three independent experiments. (Scale bar: 20 µm.) (*J* and *K*) Quantification of flipped NBD-PIP2 or NBD-PE in WT and *ATP8b1*$^{-/-}$ HePG2 cells (N = 25 cells, values are mean ± SD; **** show $P < 0.0001$ by the *t* test. (*L*) ATPase activity of ATP8B1 in presence of various lipids (300 µM). (*M*) Phospholipid concentration-dependent ATPase activity of ATP8B1. Graph representing data points of three independent experiments, values are mean ± SD and fitted by a non-linear dose-dependent curve. (*N*) Schematic diagram for PIP2 flip assay in ATP8B1 proteoliposomes vs. empty liposomes. (*O*) Sodium dithionite quenching of NBD-PIP2 on the outer side of the proteoliposomes vs. empty liposomes over 10 min, Triton-X-100 was used to quench all the remaining NBD-PIP2. (*P*) Plot showing the percentage PIP2 flipped over time in proteoliposomes vs. empty liposomes ± sodium dithionite, ±Triton-X-100, data are from three independent experiments, values are mean ± SD, **** show $P < 0.0001$ by the *t* test. (*Q*) Sodium dithionite quenching of NBD-PE on the outer side of the proteoliposomes vs. empty liposomes over 10 min, Triton-X-100 was used to quench the remaining inner leaflet NBD-PE. (*R*) Plot showing the percentage PE flip over time in proteoliposomes vs. empty liposomes ± Sodium dithionite, ±Triton-X-100. The data are from three independent experiments, values are mean ± SD, n.s, nonsignificant by the *t* test.

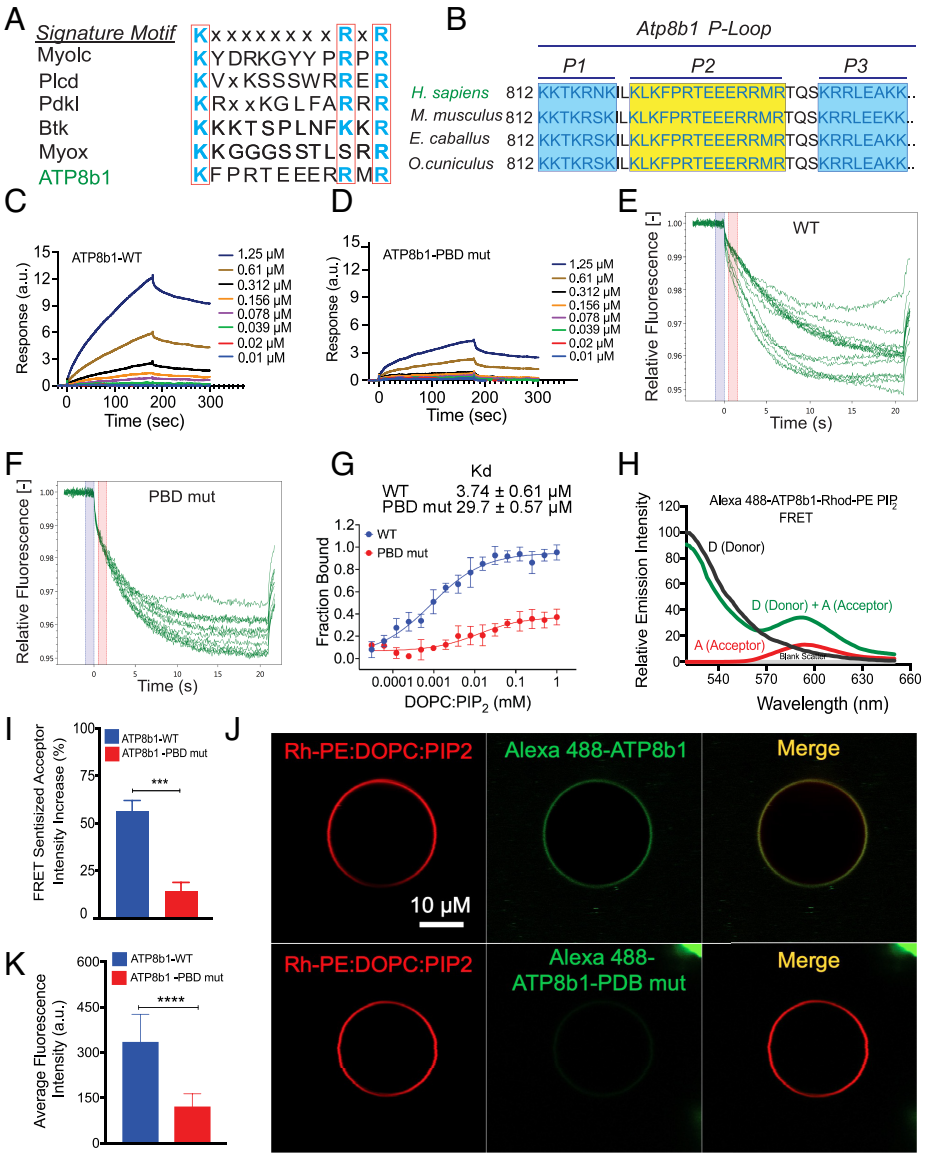

Fig. 3. ATP8B1 binds to PIP2. (*A*) Alignment of putative PIP2 binding domain of ATP8B1 with known PIP2-binding proteins. (*B*) Multiple sequence alignment of the P2 region of the P-loop of ATP8B1 (AA 812-847) showing the conserved PIP2 binding region across different species. (*C*) SPR analysis of PIP2 binding with WT-ATP8B1 (*D*) SPR analysis of PBD mutant of ATP8B1. (*E*) MST traces showing the relative fluorescence of Alexa-488 labeled WT-ATP8B1. (*F*) MST of Alexa-488 labeled PBD mutant of ATP8B1. (*G*) MST binding curve of Alexa-488 labeled WT-ATP8B1 vs. PBD mutant-ATP8B1 binding to DOPC:PIP2(95:5) liposomes. The *X*-axis shows an increasing concentration of DOPC:PIP2(95:5) liposomes. Data plotted are mean ± SE. (*H*) Representative FRET fluorescence spectra of 0.5 µM of Alexa488-labeled WT-ATP8B1 (donor) ±1 mol% Rhodamine-PE (acceptor) doped in 200 µM of DOPC:PIP2(95:5) liposomes. (*I*) FRET sensitized percentage increase in acceptor (1 mol% Rhod-PE-DOPC:PIP2) by 0.5 µM of donor Alexa 488 WT vs. PBD mutant of ATP8B1. Data plotted are mean ± SE, *** show $P < 0.001$ by the *t* test. (*J*) Microscopic GUVs of DOPC:PIP2 (95:5) doped with 1 mol% of Rhodamine PE (red fluorescence) incubated with 0.5 µM of Alexa-488 labeled (green fluorescence), with *Top* panel showing Alexa488-ATP8B1-WT on the equatorial plane of GUV vs. Alexa 488-ATP8B1-PBD mutant (*Lower* panel). (*K*) Oval profile showing quantitative analysis of the interaction between GUVs with WT or PBD-mutant of ATP8B1, ~25 GUVs were quantified for both samples and the data are presented as mean ± SE, $P < 0.0001$ with the *t* test.

is a part of the complement pathway, and ATP10A, a P4-ATPase associated with insulin resistance and diet-induced dyslipidemia (33). These data indicated crosstalk between cell signaling pathways, bile acid metabolism, and phospholipid trafficking/metabolism in ATP8B1$^{-/-}$ hepatocytes. The top altered pathways in *ATP8B1*$^{-/-}$ macrophages and monocytes included signal transduction, inflammatory and LPS responses, cholesterol/lipoprotein metabolism, and cytokine responses (*SI Appendix*, Fig. S9 *B* and *C*). The top altered genes in *ATP8B1*$^{-/-}$ macrophages included several proinflammatory genes such as IL36B, IL1α, IL1β, CXCLB, CCL3, and CCL3L1 (Fig. 4 *C* and *D*). Top downregulated genes include SLAM family members which are required for the normal function of the immune system (34) (Fig. 4 *C* and *D*). Monocytes deleted for ATP8B1 also showed altered expression of genes and pathways involved directly or indirectly in inflammation and cholesterol/bile-salt homeostasis (Fig. 4 *E* and *F* and *SI Appendix*, Fig. S9*C*). For instance, AKR1C1 and AKR1C2, which play a role in protecting from LPS-mediated injury and maintaining bile-acid homeostasis were downregulated (35). Up-regulated genes include *GAS6*, which is involved in regulating many biological processes, such as cell proliferation, efferocytosis, and apoptosis (36). Overall, these data indicated that ATP8B1 is involved in regulating immune responses, efferocytosis, and generation/release of proinflammatory cytokines.

Inflammation-resolving pathways such as efferocytosis and phagocytosis play a key role in several inflammatory diseases, and interestingly, PIP2 is also involved in these processes (36–39). We tested the status of inflammation-resolving pathways in *ATP8B1*$^{-/-}$ macrophages. THP-1 *ATP8B1*$^{-/-}$ macrophages showed significantly reduced phagocytosis of latex beads, though the binding of beads to the membrane was not impaired (Fig. 4*G* and *SI Appendix*, Fig. S9*D*), indicating that phagocytosis is impaired downstream of the binding step. In addition to latex beads, no-wash fluorogenic *Escherichia coli* bioparticles were used for quantitative measurements of phagocytosis, with the advantage being that a specific signal is obtained only from cells that ingest the particles. As shown in Fig. 4*H*, *Atp8b1*$^{-/-}$ macrophages exhibited markedly reduced engulfment of *E. coli* bioparticles (Fig. 4*H*). Similar to phagocytosis, THP-1 ATP8B1$^{-/-}$ macrophages showed markedly reduced efferocytosis of apoptotic Jurkat cells vs. WT macrophages (Fig. 4 *I* and *J*). The binding of apoptotic Jurkat cells to ATP8B1$^{-/-}$ macrophages was not impaired (Fig. 4*I*), indicating downstream defects in the efferocytic pathway. Unexpectedly, the expression of efferocytic receptor MerTK was higher in THP1-

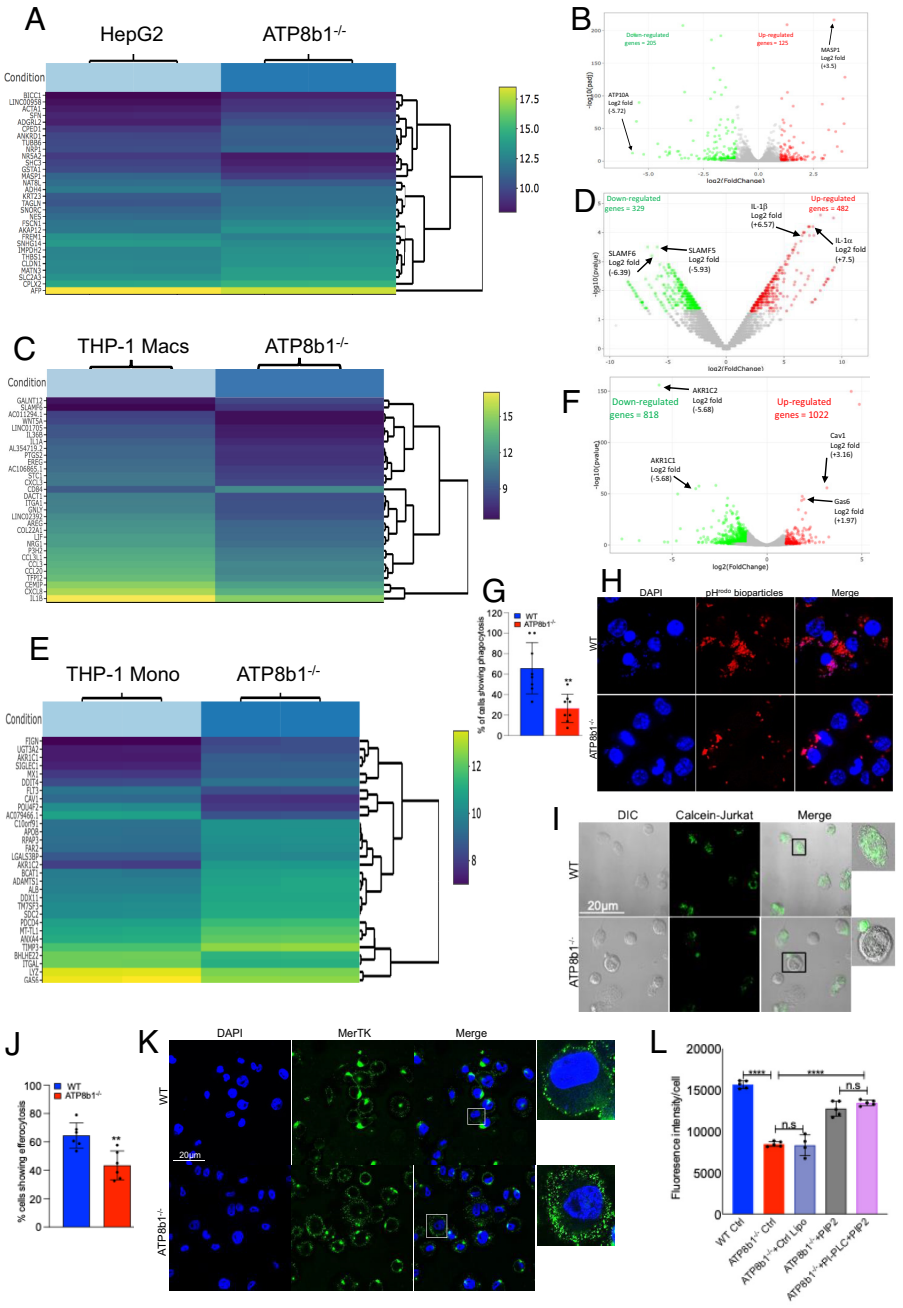

Fig. 4. Unbiased RNAseq analysis of human ATP8B1$^{-/-}$ hepatocytes, macrophages, and monocytes. (*A*) Biclustering heatmap used to visualize the top 30 genes sorted by their adjusted *P* values by plotting their log 2 transformed expression values in WT vs. *ATP8B1*$^{-/-}$ HePG2 cells. (*B*) Volcano plot showing a comparison of the global transcriptional change across the WT vs. *ATP8B1*$^{-/-}$ HepG2 cells. (*C*) Biclustering heatmap used to visualize the top 30 genes sorted by their adjusted *P* values by plotting their log 2 transformed expression values in WT vs. *ATP8B1*$^{-/-}$ THP-1 macrophages. (*D*) Volcano plot showing a comparison of the global transcriptional change across the THP-1 WT vs. *ATP8B1*$^{-/-}$ macrophages. (*E*) Biclustering heatmap used to visualize the top 30 genes sorted by their adjusted *P* values by plotting their log 2 transformed expression values in WT vs. ATP8B1$^{-/-}$ THP-1 monocytes. (*F*) Volcano plot showing a comparison of the global transcriptional change across the THP-1 WT vs. *ATP8B1*$^{-/-}$ monocyte. (*G*) Quantification of phagocytosis in THP-1-WT vs. ATP8B1$^{-/-}$ macrophages; eight independent fields were counted for each sample; the graph shows % cells showing phagocytosis per field, n > 50, mean ± SD, $^{**}P = 0.0017$ by the *t* test. (*H*) RAW264.7-WT and *Atp8b1*$^{-/-}$ macrophages were incubated with pH^{rodo} *Escherichia coli* bioparticles for 1 h at 37 °C, and phagocytosis was visualized using confocal microscopy. (*I*) THP-1-WT and *ATP8B1*$^{-/-}$ macrophages were incubated with calcein-labeled apoptotic Jurkat cells for 4 h at 37 °C, and efferocytosis was visualized using confocal microscopy. (*J*) Quantification of efferocytosis of calcein-labeled Jurkat cells, six independent fields were counted for each sample, the graph shows % cells showing efferocytosis per field, with n ≥ 60 cells per treatment group, values are mean ± SD, $^{**}P = 0.0034$ by the *t* test. (*K*) Indirect immunofluorescence for efferocytosis receptor MerTK in THP-1 WT and *ATP8B1*$^{-/-}$ macrophages. (*L*) Flow cytometry assay for quantification of phagocytic capacity of RAW264.7-WT vs. *Atp8b1*$^{-/-}$ macrophages ± PIP2, n = 4 to 5, values are mean ± SD, all columns were compared to WT column, $^{***}P = 0.0004$, $^{****}P <$ 0.0001 by ANOVA posttest.

ATP8B1$^{-/-}$ macrophages (Fig. 4*K*), indicating that reduced efferocytosis in *ATP8B1*$^{-/-}$ macrophages is not due to reduced MerTK expression. To determine whether the defective phagocytosis in *Atp8b1*$^{-/-}$ cells is due to altered PIP2 localization, *Atp8b1*$^{-/-}$ cells were supplemented with exogenous PIP2. PIP2 liposomes, instead of free PIP2, were used to ensure PIP2 distribution on both leaflets of the PM. As shown in Fig. 4*L*, PIP2 significantly increased the phagocytic capacity of *Atp8b1*$^{-/-}$ cells, though the rescue was not to the levels of WT cells. To ensure that exposed PIP2 in *Atp8b1*$^{-/-}$ cells is not interfering with the fusion of PIP2 liposomes or equal distribution of PIP2 across the PM bilayer, cells were preincubated with PI-PLC to excise external PIP2, followed by loading with PIP2 liposomes. Even under these conditions, the rescue of phagocytic capacity remained partial (Fig. 4*L*). These data indicated that altered PIP2 localization in Atp8b1$^{-/-}$ cells contributes to defective phagocytosis/efferocytosis.

ATP8B1 Regulates GSDMD Cleavage and the Formation of Membrane Pores. GSDMD promotes various inflammatory diseases by regulating the release of proinflammatory cytokines (22). Strikingly, we found that LPS exposure alone was sufficient to trigger GSDMD cleavage in human *ATP8B1*$^{-/-}$ monocytes and macrophages vs. WT controls (Fig. 5*A* and *SI Appendix*, Fig. S10*A*). Induction with secondary stimuli Nigericin led to the cleavage of GSDMD in both WT and *ATP8B1*$^{-/-}$ monocytes, but the cleavage of GSDMD was much higher in *ATP8B1*$^{-/-}$ monocytes (Fig. 5 *A* and *B*). LPS alone or LPS + Nigericin treatment led to markedly higher interleukin-1beta(IL1β) release from ATP8B1$^{-/-}$ monocytes and macrophages vs. WT controls (Fig. 5 *C* and *D*). Similar trends were observed in primary bone marrow–derived macrophages (BMDMs), where LPS + Nigericin treatment led to significantly higher GSDMD cleavage and IL1β release in BMDMs isolated from Atp8b1$^{-/-}$ mice vs. WT mice (Fig. 5 *E*–*G*). Importantly,

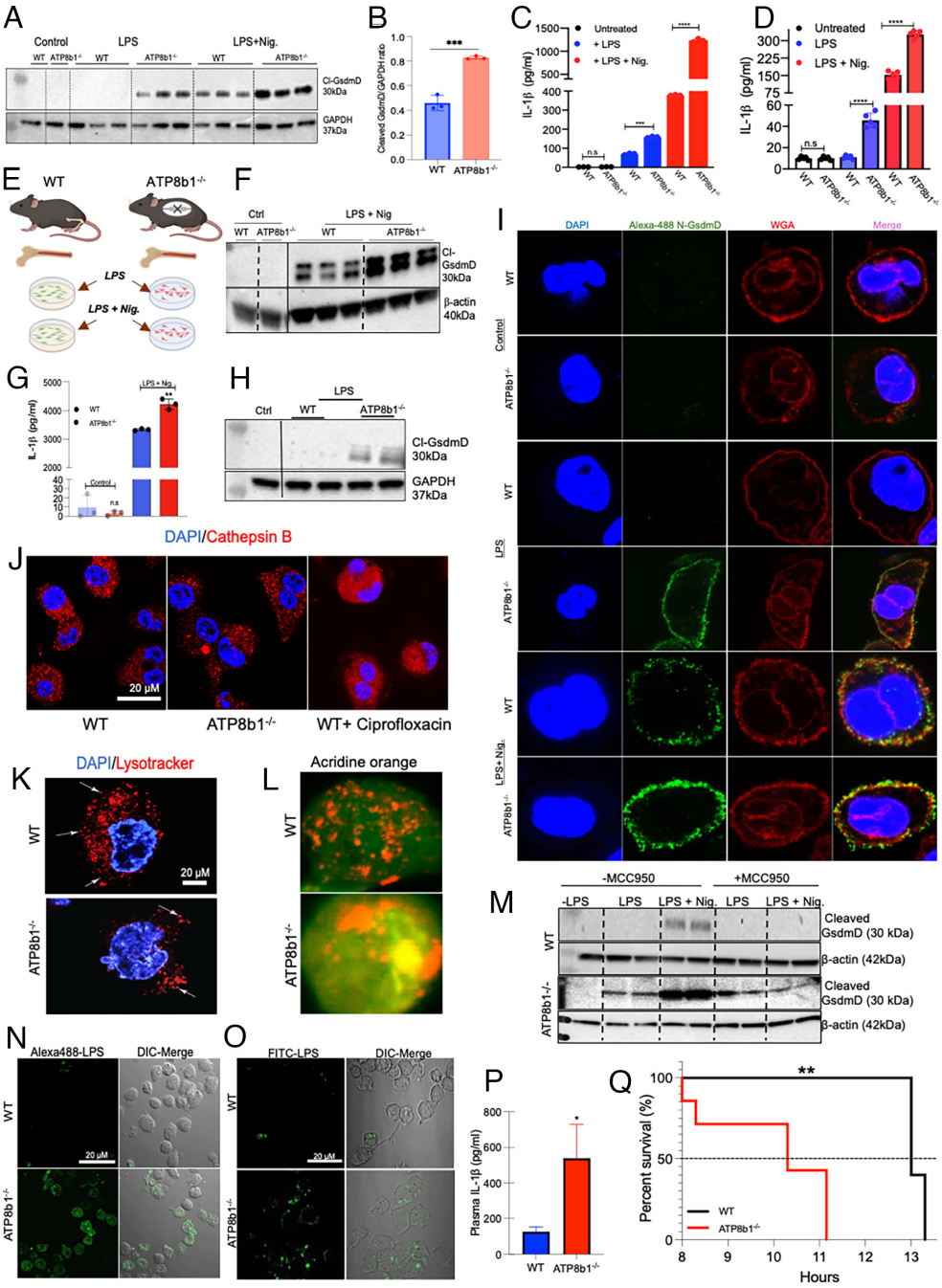

Fig. 5. ATP8B1 is a negative regulator of GSDMD cleavage. (*A*) THP-1 WT or *ATP8B1*$^{-/-}$ monocytes were treated with ±1 μg/mL of LPS for 3 h ±5 μM of nigericin for 1 h. Cell extracts were probed with human-specific cleaved GSDMD antibody, GAPDH serves as loading control, and (*B*) Graph showing quantification of western blot bands. (*C*) ELISA for measuring IL1β release in media from THP-1 WT or *ATP8B1*$^{-/-}$ monocytes, with n = 3, mean ± SD; **** show $P < 0.0001$, *** show $P < 0.001$, n.s = nonsignificant by ANOVA posttest. (*D*) ELISA for measuring IL1β release in media from THP-1 WT or *ATP8B1*$^{-/-}$ macrophages, with n = 5, mean ± SD; **** show $P < 0.0001$, n.s = nonsignificant by ANOVA posttest. (*E*) Schematic diagram showing BMDMs from WT and *Atp8b1*$^{-/-}$ mice treated with ±LPS ± Nig. (*F*) BMDMs derived from C57BL6J WT or *Atp8b1*$^{-/-}$ mice were treated with ±1 μg/mL of LPS for 3 h ±5 μM of nigericin for 1 h. Cell extracts were probed with mouse-specific cleaved GSDMD antibody, β-actin serves as loading control. (*G*) ELISA for measuring IL1β release in media from WT or *Atp8b1*$^{-/-}$ BMDMs, with n = 3, mean ± SD; $^{**}P = 0.0012$ by the *t* test. (*H*) Western blot of cleaved N-terminal fragment of GSDMD from BMDMs derived from C57BL6/J- WT or *Atp8b1*$^{-/-}$ mice were treated with ±10 μg/mL of LPS for 3 h. (*I*) Indirect immunofluorescence for N-terminal fragment of GSDMD in THP-1 WT and *ATP8B1*$^{-/-}$ macrophages with ±1 μg/mL of LPS for 3 h ±5 μM of nigericin for 1 h. Wheat Germ Agglutinin (WGA) is used to stain the membrane. (*J*) Indirect immunofluorescence for lysosomal protease Cathepsin B in THP-1 WT and *ATP8B1*$^{-/-}$ macrophages. WT cells treated with Ciprofloxacin were used as a positive control for Cathepsin B release in the cytoplasm. (*K*) THP-1 WT and ATP8B1$^{-/-}$ macrophages were stained with Lysotracker Deep Red (75 nM for 2 h), followed by 3× washing with PBS and fixing. Cells were imaged using high-resolution STED microscopy. (*L*) THP-1 WT and ATP8B1$^{-/-}$ macrophages were incubated with Acridine orange (2.6 μM for 10 min), followed by washing, fixing, and imaging of cells using confocal microscopy. (*M*) THP-1 WT or *ATP8B1*$^{-/-}$ macrophages were treated with ±MCC950 (10 μM) ±LPS ± Nigericin. Samples were probed using an antibody specific for cleaved N-terminal fragment of GSDMD. β-actin was used as a loading control. (*N*) THP-1 WT or *ATP8B1*$^{-/-}$ monocytes were incubated with Alexa488-labeled LPS (1 μg/mL for 3 h) and imaged using confocal microscopy. (*O*) RAW 264.7-WT or ATP8b1$^{-/-}$ macrophages were incubated with FITC-LPS (1 μg/mL for 3 h) and imaged using confocal microscopy. (*P*) C57BL6J WT or *Atp8b1*$^{-/-}$ mice (WT n = 5, ATP8b1$^{-/-}$ n = 7,) were injected intraperitoneally with a lethal dose of LPS (25 mg/kg). ELISA showing plasma IL1β post 4 h LPS injection. (*Q*) Survival curve for WT and *Atp8b1*$^{-/-}$ mice, $P = 0.0033$ by the log-rank test.

similar to human *ATP8B1*$^{-/-}$ immune cells, exposure to LPS alone induced cleavage of GSDMD in BMDMs isolated from Atp8b1$^{-/-}$ mice vs. WT mice (Fig. 5*H*). To determine whether cleavage of GSDMD indeed leads to physiological consequences, the status of GSDMD membrane pores in *ATP8B1*$^{-/-}$ vs. WT cells was assessed. As expected, the untreated WT or *ATP8B1*$^{-/-}$ cells showed no GSDMD pores on the PM. Exposure to LPS alone led to robust GSDMD pores on the PM of *ATP8B1*$^{-/-}$ cells, while no GSDMD pores were observed in WT cells (Fig. 5*I*). Furthermore, the *ATP8B1*$^{-/-}$ cells showed markedly increased GSDMD membrane pores vs. WT cells upon assembly of NLRP3 inflammasome by LPS + Nig. treatment (Fig. 5*I*). The basal NLRP3 expression was higher in *ATP8B1*$^{-/-}$ macrophages (*SI Appendix*, Fig. S10*B*), but there were no differences in basal or LPS-induced nuclear localization of NF-kB in *ATP8B1*$^{-/-}$ cells (*SI Appendix*, Fig. S10*C*), indicating that increased NLRP3 expression is not due to enhanced transcription. To determine the mechanism for LPS-induced GSDMD cleavage, we tested whether *ATP8B1*$^{-/-}$ cells have any endogenous anomalies that can serve as a second signal for inflammasome assembly and GSDMD cleavage. There was no cytoplasmic release of lysosomal proteins such as Cathepsin B, a potent inducer of inflammasome activity, in *ATP8B1*$^{-/-}$ vs. WT cells (Fig. 5*J* and *SI Appendix*, Fig. S11). Also, no differences were found in *ATP8B1*$^{-/-}$ vs. WT cells for basal cytoplasmic or starvation-induced nuclear localization of transcription factor EB (TFEB), a master regulator of lysosomal biogenesis (*SI Appendix*, Fig. S12). These data indicated that lysosomal generation and lysosomal membrane integrity were not compromised in *ATP8B1*$^{-/-}$ cells.

Though no differences were found in lysosomal membrane integrity, high-resolution stimulated emission depletion (STED) microscopy showed a significantly lower lysotracker staining in *ATP8B1*$^{-/-}$ vs. WT macrophages (Fig. 5*K* and *SI Appendix*, Fig. S13 *A* and *B*). Lysotracker accumulates in the acidic organelle; thus, we tested whether lysosomal pH was altered in *ATP8B1*$^{-/-}$ macrophages. Acridine orange was used, a metachromatic dye that emits green fluorescence in monomeric form and red fluorescence upon accumulation in the form of stacks in acidic lysosomes. The lysosomal pH was significantly less acidic in *ATP8B1*$^{-/-}$ vs. WT macrophages, with ~55% reduction in red fluorescence per cell (n > 40 cells per group) (Fig. 5*L* and *SI Appendix*, Fig. S14 *A* and *B*).

Noncanonical GSDMD Cleavage and Increased Susceptibility of Atp8b1G308V/G308V Mice toward LPS-Induced Mortality. To determine whether ATP8B1 regulates GSDMD cleavage via canonical inflammasome pathway, cells were pretreated with MCC950, a potent NLRP3 inhibitor. As shown in Fig. 5*M*, the GSDMD was still cleaved in THP-1 *ATP8B1*$^{-/-}$ macrophages treated with LPS alone, indicating NLRP3-independent cleavage of GSDMD. Upon LPS + Nigericin treatment, MCC950 inhibited GSDMD cleavage by the NLRP3, but not the LPS-only component (Fig. 5*M*). As expected, MCC950 completely abolished GSDMD cleavage in WT macrophages (Fig. 5*M*). These data indicate that the LPS-induced cleavage of GSDMD in *ATP8B1*$^{-/-}$ cells is independent of the caspase-1/NLRP3 pathway. In contrast, Ac-FLTD-CMK, a potent and selective inhibitor of caspases-1/4/5, completely blocked LPS-induced cleavage of GSDMD in *ATP8B1*$^{-/-}$ cells (*SI Appendix*, Fig. S14*C*). Mechanistically, LPS penetrated the membrane and gained access to the cytoplasm in THP-1 *ATP8B1*$^{-/-}$ monocytes as well as in Atp8b1$^{-/-}$ mouse macrophages vs. WT controls (Fig. 5 *N* and *O*), leading to noncanonical inflammasome activation and GSDMD cleavage. To determine whether the *Atp8b1*$^{-/-}$ mice (10, 40) are more susceptible to LPS-induced inflammation, a lethal dose of LPS was injected in WT and *Atp8b1*$^{-/-}$ mice. As shown in Fig. 5*P*, the plasma IL1β levels were ~fourfold higher in *Atp8b1*$^{-/-}$ mice injected with LPS vs. WT mice. Furthermore, the *Atp8b1*$^{-/-}$ mice showed a mean survival rate of only ~10.30 h vs. ~13 h of WT mice (Fig. 5*Q*), indicating increased susceptibility of *Atp8b1*$^{G308V/G308V}$ mice to sepsis-induced mortality.

Altered Biomechanical Properties of ATP8B1$^{-/-}$ PM Can Be Restored by PIP2. Phagocytosis and efferocytosis are shown to be affected by the biophysical properties of cell membrane (41–43). Atomic Force Microscopy (AFM) analysis revealed that the biomechanical properties of WT THP-1 macrophages were Young's modulus (E_Y) = 415.1 ± 141.7 Pa, adhesion force (F_{ad}) = 518.8 ± 196.1 pN, tether force (F_T) = 213.3 ± 72.8 pN, apparent membrane tension (T_M) = 2,705 ± 1,254 pN/μm, and radius of tether (R_T) = 6.9 ± 2 nm, which were used as reference compared to test cases. Significant decreases in E_Y and R_T, and concomitant increases in F_{ad}, F_T, and T_M, were noted in *ATP8B1*$^{-/-}$ cells compared to WT cells (Fig. 6 *A–I*). To investigate whether altered biomechanical properties are due to the altered distribution of PIP2 across plasma membrane (PM) bilayer in *ATP8B1*$^{-/-}$ cells, PIP2 was supplemented via liposomes. Unlike nonmicellar PIP2, PIP2 liposomes can diffuse in the PM and distribute equally to both sides of the PM. PIP2 delivery from DOPC (denoted as +PIP2) did not significantly alter the E_Y, F_{ad}, F_T, and T_M of WT cells compared to the delivery of DOPC alone (denoted as -PIP2) or compared to the WT cells that did not receive DOPC (Fig. 6 *B–J*). Interestingly, the average E_Y and R_T significantly increased in ATP8b1$^{-/-}$ macrophages treated with DOPC-PIP2 vs. DOPC alone, while F_T, T_M and F_{ad} values significantly decreased, in ATP8b1$^{-/-}$ macrophages treated with DOPC-PIP2 vs. DOPC alone ($P < 0.001$ vs. *ATP8B1*$^{-/-}$ in all the cases; $P < 0.001$ for *ATP8B1*$^{-/-}$ + PIP2 vs. ATP8B1$^{-/-}$—PIP2) (Fig. 6 *B–J*). We evaluated whether osmotic pressure differences across the membrane (ΔP) might be contributing to the changes in tether forces. The membrane tension on the cell could be related to ΔP using the Young–Laplace equation ($\Delta P \cong (2\,T_M/(R_T))$ (44). For the 2 nN force imparted on the cells by the AFM beaded-tip, the ΔP values for WT and ATP8B1$^{-/-}$ cells were 772.8 ± 37 kPa and 2,999 ± 79 kPa, respectively ($P < 0.001$ for WT vs. ATP8B1$^{-/-}$), suggesting a significant increase in osmotic pressure difference across the PM in ATP8B1 knockout cells. Addition of DOPC ± PIP2 did not affect ΔP in WT cells ($P > 0.1$ vs. WT). However, the ΔP values were 1,071.4 ± 80.9 kPa and 464.7 ± 27 kPa in ATP8B1$^{-/-}$ cells with the addition of DOPC-PIP2 and DOPC+PIP2 liposomes, respectively, suggesting that the addition of PIP2 dropped the ΔP levels similar to that in WT cells. A similar trend was observed in HEK293 cells, where deletion of ATP8B1 decreased Young's modulus (E_Y), indicating more elastic PM vs. WT cells (*SI Appendix*, Fig. S15 *A* and *B*). These data were further confirmed in various *ATP8B1*$^{-/-}$ cell lines by measuring the dipole potential of PM by using Di-8-ANEPPS dye (Fig. 6*K*). The dipole potential of PM in ATP8B1$^{-/-}$ cells was significantly lower vs. corresponding WT cells (Fig. 6*L*). We also visualized the distribution of Di-8-ANEPPS dye via STED Super-Resolution Imaging (STEDYCON) microscopy using a dual-wavelength ratiometric imaging approach. The 3D surface plot depicting the fluorescence intensity of Di-8-ANEPPS illustrated a more localized presence of the dye on the PM of WT cells vs. diffused distribution in *ATP8B1*$^{-/-}$ cells (Fig. 6*M*). To determine whether the change in dipole potential is due to PIP2 redistribution in *ATP8B1*$^{-/-}$ cells, cells were supplemented with PIP2 liposomes. As shown in Fig. 6*N*, PIP2 supplementation restored membrane dipole potential in a dose-dependent manner.

Discussion

Several recent and elegant studies highlighted the emerging roles of ATP8B1 in lipid homeostasis (19, 29, 45), and pointed toward the intricate relation between ATP8B1 and phosphoinositide metabolism (18), but the mechanistic details of the interplay between ATP8B1 and phosphatidylinositol phosphates (PIPs) metabolism are not clear.

Using homozygous *ATP8B1*$^{-/-}$ in a variety of cell types, we show that PIP2 is exposed at the exoplasmic side of the PM bilayer in *ATP8B1*$^{-/-}$ cells. PIP2 exposure was further augmented in *Atp8b1*$^{-/-}$ cells expressing ABCA1 (Fig. 1), indicating that ATP8B1 and ABCA1 are involved in flip-flop of PIP2, and cells may coregulate the expression of these proteins to maintain appropriate PIP2 levels across PM. In support of this argument, previous studies have shown *the* coregulation of ATP8B1 and ABCA1 by microRNA MiR-33 (46–50). A time-lapse live cell imaging microscopy-based assay was used to determine ATP8B1 mediated translocation of exogenous Bodipy-TMR labeled PIP2. Boron dipyrromethene (BODIPY) is a highly lipophilic neutral fluorophore that emits fluorescence only when it is embedded within a hydrophobic lipid environment. Thus, Bodipy-PIP2 remains nonfluorescent in media until it latches and gets inserted in the PM lipid bilayer. In WT cells, the Bodipy-PIP2 binds to the outer layer and is then translocated to the inner leaflet by ATP8B1, leading to a strong Bodipy signal at the PM. The *ATP8B1*$^{-/-}$ cells, which are defective in

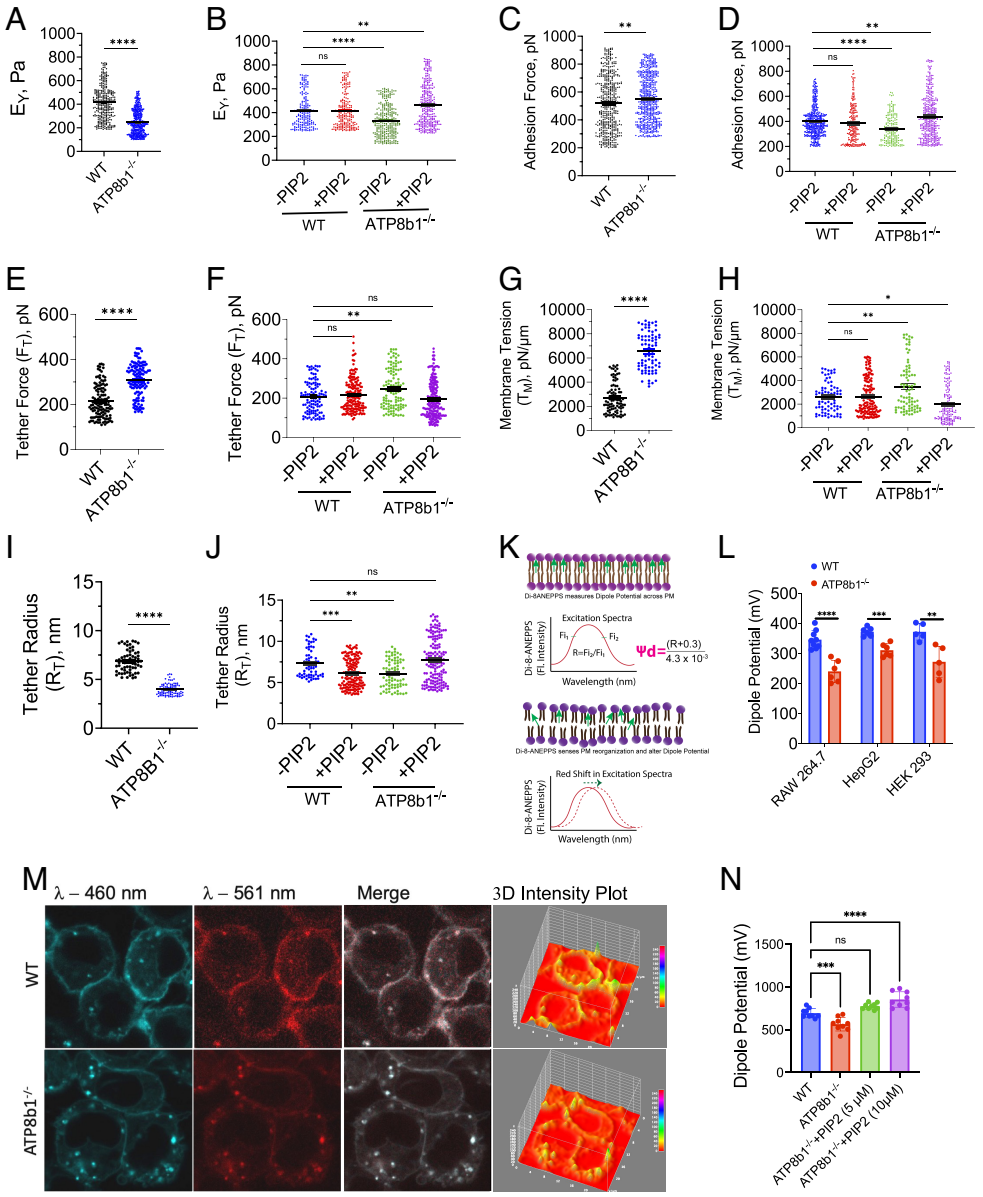

Fig. 6. Altered biomechanical properties of ATP8B1$^{-/-}$ cells can be restored by PIP2 supplementation. The Young's modulus (E_Y, Pa) representing stiffness of (*A*) WT and *ATP8B1*$^{-/-}$ cells, and (*B*) WT ± PIP2 and *ATP8B1*$^{-/-}$ cells ± PIP2. Adhesive forces (F_{ad}) between the AFM tip and the cell surface for (*C*) WT and *ATP8B1*$^{-/-}$ cells, and (*D*) WT ± PIP2 and *ATP8B1*$^{-/-}$ cells ± PIP2. Membrane tether forces (F_T), for (*E*) WT and *ATP8B1*$^{-/-}$ cells, and (*F*) WT ± PIP2 and *ATP8B1*$^{-/-}$ cells ± PIP2. From the F_T values, the apparent PM tension (T_M) noted for (*G*) WT and *ATP8B1*$^{-/-}$ cells, and (*H*) WT ± PIP2 and *ATP8B1*$^{-/-}$ cells ± PIP2. The tether radius (R_T) was obtained from the F_T values for (*I*) WT and *ATP8B1*$^{-/-}$ cells, and (*J*) WT ± PIP2 and *ATP8B1*$^{-/-}$ cells ± PIP2. In all cases, data are from three replicates, with $323 \le n \le 493$ cells for E_Y values, $182 \le n \le 561$ cells for F_{ad} values, and $64 \le n \le 201$ for F_T, T_M and R_T values. Circles represent the data points and lines represent the mean ± SE. $^*P < 0.01$, $^{**}P < 0.001$, $^{****}P < 0.0001$. (*K*) Schematic diagram depicting intercalating of charge-shift probe Di-8-ANEPPS to the cell membrane and excitation spectra showing changes in the orientation of the probe in the membrane bilayer. (*L*) Dipole potential of the PM in various WT vs. *ATP8B1*$^{-/-}$ cells. Bar graphs showing independent triplicates; data are mean ± SE, $^{**}P < 0.01$, $^{***}P < 0.001$, $^{****}P < 0.0001$ by the *t* test. (*M*) Representative STEDYCON micrograph showing Di-8-ANEPPS labeled RAW 264.7 WT and *Atp8b1*$^{-/-}$ cells (Ext: 460 nm, *Left* panel, Ext: 561 nm *Middle* panel, and the emission bandpass was fixed at 670 nm). The 3D intensity plot corresponding to the fluorescence intensity ratio R (color-coded) was calculated using ImageJ. (*N*) Dipole potential of WT RAW 264.7 compared with *Atp8b1*$^{-/-}$ cells ± supplementation with 5 μM and 10 μM PIP2 liposomes, the bar graph is showing values with mean ± SE; data are mean ± SE, $^{***}P < 0.001$, $^{****}P < 0.0001$, n.s.= nonsignificant by the *t* test.

flipping PIP2, Bodipy-PIP2 does seem to transiently bind to the cell-surface (Movies S1–S4) but quickly gets exchanged back to the media, leading to weak Bodipy-PIP2 signal at the PM (Fig. 2). Importantly, PIP2 flip defect is specific as the flip of PE was not affected. An independent method allowing differentiation between ATPase-mediated flip of NBD-lipids and endocytosis-mediated entry of NBD-lipids in the cells also showed that ATP8B1 is essential for flipping PIP2. Interestingly, the kinetics of PIP2 flip was cell-type dependent, with macrophages showing much faster PIP2 flip vs. hepatocytes (Fig. 2). The physiological relevance of differential kinetics is not clear, but we speculate that cells involved in PIP2-mediated signaling pathways may regulate the rate of PIP2 flip to modulate signaling events. The crosstalk between ATP8B1 and PIP2 trafficking/metabolism was further strengthened by our data showing that ATP8B1 contains a conserved PIP2 binding domain, which allows direct binding between ATP8B1 and PIP2 (Fig. 3). Mutations in the PIP2 binding domain of ATP8B1, such as R833W, are found in human patients (51), but the physiological role of this domain is not yet described. We speculate that PIP2 binding serves as a regulatory mechanism for modulating ATP8B1 activity. For instance, high levels of PIP2 at the inner leaflet of the PM can promote PIP2 binding to ATP8B1 and may result in dampened PIP2 flip activity to avoid excessive enrichment of PIP2 at the inner bilayer of PM. ATP8B1 also plays a physiological role in hearing, as ATP8B1 mutation causes hearing loss, associated with progressive degeneration of cochlear hair cells (15). Interestingly, like ATP8B1, PIP2 is also critical for mechanical transduction and adaptation of hair cells (16, 17), indicating an intricate link between PIP2 and the physiological functions of ATP8B1.

PFIC1 patients also show multiple extrahepatic inflammatory features that are independent of cholestasis and persist even after a liver transplant (52). ATP8B1 was shown to regulate the polarization of HMDMs into M2c (21). Thus, ATP8B1 may be involved in regulating the inflammatory activity of immune cells. We performed a comprehensive and unbiased analysis of transcriptome-wide alterations in *ATP8B1*$^{-/-}$ macrophages as well as monocytes and found clear enrichment of several proinflammatory cytokines (Fig. 4). Efferocytosis and phagocytosis play a vital role in resolution of inflammation (36). The macrophages

lacking ATP8B1 showed marked defects in efferocytosis/phagocytosis (Fig. 4). Surprisingly, the cell-surface expression of efferocytic receptor MerTK was found to be higher in *ATP8B1*$^{-/-}$ macrophages. The up-regulated MerTK expression in *ATP8B1*$^{-/-}$ macrophages may be a compensatory mechanism to counter defective efferocytosis, but this seems inadequate to restore the efferocytic ability of *ATP8B1*$^{-/-}$ macrophages.

Previous studies have shown crosstalk between PIP2 and cholesterol trafficking (53, 54). Interestingly, PIP2 supplementation in the form of liposomal fusion, which can lead to equal distribution of PIP2 across both layers of PM, seems to partially rescue the phagocytic capacity of ATP8B1$^{-/-}$ macrophages. Thus, the depletion of PIP2 from the inner leaflet of the PM, rather than the exposure of PIP2 at the cell surface, seems responsible for the defective phagocytic capacity of *ATP8b1*$^{-/-}$ cells. The partial rescue could also be due to PIP2 trafficking to intracellular membranes over time, rather than sticking to PM. Thus, defective phagocytosis and efferocytosis may serve as another contributory factor for persistent chronic inflammation in PFIC1 patients.

Several studies have highlighted the major role of pyroptosis executor GSDMD in promoting a variety of inflammatory diseases (22). Strikingly, LPS exposure alone, in the absence of any secondary signal, led to GSDMD cleavage and IL1β release in *ATP8B1*$^{-/-}$ monocytes and macrophages (Fig. 5). No changes were observed in basal or LPS-induced nuclear translocation of NF-kB, ruling out the possibility of increased transcription of pro-IL1β. No differences were observed in basal or starvation-induced nuclear translocation of TFEB, a master regulator of lysosomal biogenesis (55, 56). There was no release of Cathepsin B from lysosomes to the cytoplasm in *ATP8B1*$^{-/-}$ cells (Fig. 5), indicating that the integrity of the lysosomal membrane was also maintained. Lysosomal pH was less acidic in *ATP8B1*$^{-/-}$ cells, thus ATP8B1 may have a direct or indirect role in regulating the expression/function of proton pumps on the lysosomal membrane.

We found that LPS can access the cytoplasm of the *ATP8B1*$^{-/-}$ cells, leading to noncanonical inflammasome-dependent GSDMD cleavage and IL1β release (Fig. 5). We speculate that this observation is of physiological relevance, as humans are always exposed to low levels of LPS (either from gut microbiota or other external sources). Low LPS exposure in healthy humans may not cause major adverse effects, but in PFIC1 patients or in patients carrying heterozygous mutations of ATP8B1, LPS may diffuse in immune cells and cause GSDMD cleavage and IL1β release, leading to chronic inflammation. In support of this notion, the *Atp8b1*$^{G308V/G308V}$ *mouse* model exposed to LPS showed higher plasma IL1β levels and a lower survival rate.

We also found markedly higher IL-1β release in *ATP8B1*$^{-/-}$ monocytes and macrophages upon LPS + Nigericin treatments (Fig. 5), indicating that noncanonical GSDMD cleavage can subsequently activate the canonical NLRP3 inflammasome pathway, leading to increased cleavage of IL1β and subsequently increased IL1β release via GSDMD membrane pores. Several elegant studies have pointed toward the role of ATP8B1 in inflammation via various mechanisms (57–59), and our data showing negative regulation of GSDMD cleavage by ATP8B1 provides mechanistic details on inflammatory manifestations of PFIC1.

The AFM analysis pointed toward more elastic membrane properties of *ATP8B1*$^{-/-}$ cells vs. WT cells, and the addition of PIP2 enhanced their stiffness to levels seen in WT cells. The E_Y, F_T, F_{ad}, T_M and R_T of THP-1 ATP8b1$^{-/-}$ macrophages were markedly different from WT THP-1 cells (43, 60). Still, importantly, these alterations in membrane properties do not seem responsible for general defective phospholipid flip, as the PE flip was unaffected. Rather, the defective PIP2 localization in ATP8B1$^{-/-}$ cells seems to confer altered biophysical properties of PM. This notion is supported by data showing that PIP2 supplementation and enrichment of PIP2 at the PM can restore some of the defects in membrane properties of *ATP8B1*$^{-/-}$ cells. Thus, we speculate that in addition to increased PIP2 exposure, the altered biophysical properties of the PM in *ATP8B1*$^{-/-}$ cells may also be involved in promoting excessive cholesterol extraction by bile salts as well as in allowing formation of excessive GsdmD membrane pores, leading to damaged hepatic canalicular membrane and inflammatory manifestations.

Taken together, our data identify ATP8B1 as the first reported PIP2 flippase from any system and as a negative regulator of GSDMD cleavage (*SI Appendix*, Fig. S16). Further work is required to determine whether and how PIP2 binding regulates ATP8B1 function. Preclinical studies are needed to determine whether blocking GSDMD cleavage or pore-forming activity can serve as a therapeutic target for the treatment of extrahepatic manifestations in PFIC1 patients.

Materials and Methods

A detailed description of the Materials and Methods used in this study is provided in *SI Appendix, Supplemental Materials and Methods*. Brief methods are summarized below.

Cell Culture and Reagents. RAW264.7, HepG2, THP-1, and HEK293 cells were from American Type Culture Collection (ATCC) and were cultured in appropriate media containing the required growth factors and antibiotics. Mouse BMDMs were cultured as described earlier (61). Description in *SI Appendix, Supplemental Materials and Methods*.

Mouse genotyping. C57BL/6J-Atp8b1^{tm1Nbf}/Mmcd mice (10, 40) were genotyped using primer pairs designed to differentiate WT, heterozygous, and homozygous mutations. Following primer pairs were used: MUS-IR-5 GGTAACTAATACACTAGATAC, MUS-IF-1 AATACCCCAAGCCTA ACG, MUS-IR-8 ACATCCATCCCGTTAGGC, G923T-WT-F1 CACCGATGTCTGCCA TGG, G923T-MUT-F1 CACCGATGTCTGCCATGT.

Quantification of cell-surface PIP2. Cell surface PIP2 levels were determined by flow cytometry, confocal laser scanning microscopy, and fluorescent spectroscopy using SpectraMax® i3 Multi-Mode Detection Platform (Molecular Devices). Description in *SI Appendix, Supplemental Materials and Methods*.

PIP2 localization at the inner leaflet of the PM. HepG2-WT or HepG2-*ATP8B1*$^{-/-}$ cells were stably transfected with fluorescent PIP2 reporter (2X-PH-PLC-eGFP, Addgene#35142), and PIP2 localization was determined by confocal microscopy and images were analyzed by using line-profile (ImageJ). Description in *SI Appendix, Supplemental Materials and Methods*.

PIP2 Flip Assay. Flip assay was performed in HepG2 WT and HepG2-*ATP8b1*$^{-/-}$ or RAW264.7 WT and RAW264.7-*Atp8b1*$^{-/-}$ cells Description in *SI Appendix, Supplemental Materials and Methods*. Confocal microscopy-based method for distinguishing endocytosis and NBD-lipid flip was performed following the established protocol (27).

ATP8B1 Protein Purification from Baculovirus Transfected Insect Cells. N-terminal GST-tagged human *ATP8B1* (NM_001374385) construct was codon optimized for expression in insect cells. The purified protein was stored at −80 °C for subsequent experiments. Description in *SI Appendix, Supplemental Materials and Methods*.

Preparation of proteoliposomes and lipid flip-assay. Purified ATP8B1 was reconstituted in destabilized liposomes at a lipid-to-protein molar ratio of 80:1. The flippase activity of ATP8b1 was assessed following the established protocols (29, 30).

Fluorescence Labeling of ATP8B1 Protein. WT ATP8B1 or PBD mutant of ATP8B1 were labeled using the Zip-Alexa Fluor 488 labeling Kit according to the manufacturer's protocol. Description in *SI Appendix, Supplemental Materials and Methods*.

Preparation of LUVs. LUVs were prepared using an extruder set with a heating block following the manufacturer's protocol. Description in *SI Appendix, Supplemental Materials and Methods*.

SPR. The binding kinetics of PIP2 with different isoforms of ATP8B1 were analyzed using a BiacoreS200 instrument (Cytiva # 29136649). A detailed description is provided in *SI Appendix, Supplemental Materials and Methods*.

MST. MST experiments were performed to determine the binding affinity (K_d) of ATP8B1 WT and ATP8B1 PBD mutant with PIP2. Description in *SI Appendix, Supplemental Materials and Methods*.

ATP8B1–PIP2 Interaction Using GUVs. GUVs were formed by electroformation by using Vesicle Prep Pro Station, Nanion, Germany, and lipid–protein interaction was determined as described in *SI Appendix, Supplemental Materials and Methods*.

qRT-PCR assay. Quantitative real-time PCR amplification was performed using TaqMan Universal PCR Master Mix and gene-specific primers in a Quant Studio 3 Real-Time PCR system. Description in *SI Appendix, Supplemental Materials and Methods*.

Western blotting. Western blot analysis was performed on protein extracts prepared using MPER lysis buffer ± various treatment conditions. Description in *SI Appendix, Supplemental Materials and Methods*.

Indirect immunofluorescence. THP-1 cells were differentiated into macrophages and probed with different antibodies. Description in *SI Appendix, Supplemental Materials and Methods*.

Efferocytosis assay. THP-1 monocytes were differentiated into macrophages, followed by efferocytosis assay. Description in *SI Appendix, Supplemental Materials and Methods*.

IL-1β ELISA. THP-1 cells were treated with LPS (1 μg/mL) for 3 h and with Nigericin (5 μM) for 1 h and IL-1β was measured using a human-specific IL-1β enzyme-linked immunosorbent assay (ELISA) kit. Description in *SI Appendix, Supplemental Materials and Methods*.

Acridine orange and lysotracker staining. THP-1 macrophages were treated with acridine orange or lysotracker dye, followed by microscopy. Description in *SI Appendix, Supplemental Materials and Methods*.

AFM and Dipole Potential. THP-1 macrophages were subjected to AFM analysis as previously described (43). Young's moduli (modulus of elasticity or stiffness) of the cells were determined using a Hertz model (62). Description in *SI Appendix, Supplemental Materials and Methods*.

Data, Materials, and Software Availability. All study data are included in the article and/or supporting information.

ACKNOWLEDGMENTS. This work is supported by NIH-NHLBI-RO1-HL148158, American Heart Association Transformational Project Award 23TPA1063910, and Cleveland State University startup funds to K.G. C.R.K is supported by NSF (1337859) and J.D.S is supported by NIH-RO1-HL156499. We acknowledge help from Dr. Smarajit Bandyopadhyay from Cleveland Clinic Molecular Biotechnology Core for SPR and MST experiments.

Author affiliations: [a]Center for Gene Regulation in Health and Disease, Cleveland State University, Cleveland, OH 44115; [b]Department of Biological, Geological, and Environmental Sciences, Cleveland State University, Cleveland, OH 44115; [c]Department of Cardiovascular and Metabolic Sciences, Lerner Research Institute, Cleveland Clinic, Cleveland, OH 44195; [d]Department of Chemical and Biomedical Engineering, Cleveland State University, Cleveland, OH 44115; and [e]Department of Physiology and Biophysics, Case Western Reserve University School of Medicine, Cleveland, OH 44106

1. L. N. Bull, R. Morotti, J. E. Squires, "ATP8B1 deficiency" in *GeneReviews((R))*, M. P. Adam *et al.*, Eds. (GeneReviews, Seattle, WA, 1993).
2. L. N. Bull *et al.*, Genetic and morphological findings in progressive familial intrahepatic cholestasis (Byler disease [PFIC-1] and Byler syndrome): Evidence for heterogeneity. *Hepatology* **26**, 155–164 (1997).
3. M. P. Czech, PIP2 and PIP3: Complex roles at the cell surface. *Cell* **100**, 603–606 (2000).
4. K. Mandal, Review of PIP2 in cellular signaling, functions and diseases. *Int. J. Mol. Sci.* **21**, 8342–8362 (2020).
5. K. Gulshan *et al.*, PI(4, 5)P2 is translocated by ABCA1 to the cell surface where it mediates apolipoprotein A1 binding and nascent HDL assembly. *Circ. Res.* **119**, 827–838 (2016).
6. O. Vivas, S. A. Tiscione, R. E. Dixon, D. S. Ory, E. J. Dickson, Niemann-pick type C disease reveals a link between lysosomal cholesterol and PtdIns(4,5)P2 that regulates neuronal excitability. *Cell Rep.* **27**, 2636–2648.e4 (2019).
7. J. P. Deppe *et al.*, The wheat ABC transporter Lr34 modifies the lipid environment at the plasma membrane. *J. Biol. Chem.* **293**, 18667–18679 (2018).
8. V. A. van der Mark, R. P. Elferink, C. C. Paulusma, P4 ATPases: Flippases in health and disease. *Int. J. Mol. Sci.* **14**, 7897–7922 (2013).
9. J. P. Andersen *et al.*, P4-ATPases as phospholipid flippases: Structure, function, and enigmas. *Front. Physiol.* **7**, 275 (2016).
10. C. C. Paulusma *et al.*, Atp8b1 deficiency in mice reduces resistance of the canalicular membrane to hydrophobic bile salts and impairs bile salt transport. *Hepatology* **44**, 195–204 (2006).
11. S. Y. Cai *et al.*, ATP8B1 deficiency disrupts the bile canalicular membrane bilayer structure in hepatocytes, but FXR expression and activity are maintained. *Gastroenterology* **136**, 1060–1069 (2009).
12. C. C. Paulusma, D. R. de Waart, C. Kunne, K. S. Mok, R. P. Elferink, Activity of the bile salt export pump (ABCB11) is critically dependent on canalicular membrane cholesterol content. *J. Biol. Chem.* **284**, 9947–9954 (2009).
13. A. Groen *et al.*, Complementary functions of the flippase ATP8B1 and the floppase ABCB4 in maintaining canalicular membrane integrity. *Gastroenterology* **141**, e1921–e1924 (2011).
14. P. M. Verhulst *et al.*, A flippase-independent function of ATP8B1, the protein affected in familial intrahepatic cholestasis type 1, is required for apical protein expression and microvillus formation in polarized epithelial cells. *Hepatology* **51**, 2049–2060 (2010).
15. J. M. Stapelbroek *et al.*, ATP8B1 is essential for maintaining normal hearing. *Proc. Natl. Acad. Sci. U.S.A.* **106**, 9709–9714 (2009).
16. M. Hirono, C. S. Denis, G. P. Richardson, P. G. Gillespie, Hair cells require phosphatidylinositol 4,5-bisphosphate for mechanical transduction and adaptation. *Neuron* **44**, 309–320 (2004).
17. T. Effertz, L. Becker, A. W. Peng, A. J. Ricci, Phosphoinositol-4,5-bisphosphate regulates auditory hair-cell mechanotransduction-channel pore properties and fast adaptation. *J. Neurosci.* **37**, 11632–11646 (2017).
18. C. F. Puts, G. Lenoir, J. Krijgsveld, P. Williamson, J. C. Holthuis, A P4-ATPase protein interaction network reveals a link between aminophospholipid transport and phosphoinositide metabolism. *J. Proteome Res.* **9**, 833–842 (2010).
19. T. Dieudonne *et al.*, Activation and substrate specificity of the human P4-ATPase ATP8B1. *Nat. Commun.* **14**, 7492 (2023).
20. E. D. Pfister *et al.*, Extrahepatic manifestations of progressive familial intrahepatic cholestasis syndromes: Presentation of a case series and literature review. *Liver Int.* **42**, 1084–1096 (2022).
21. A. Mizutani *et al.*, Assessment of adenosine triphosphatase phospholipid transporting 8B1 (ATP8B1) function in patients with cholestasis with ATP8B1 deficiency by using peripheral blood monocyte-derived macrophages. *Hepatol. Commun.* **5**, 52–62 (2021).
22. S. M. Man, T. D. Kanneganti, Gasdermin D: The long-awaited executioner of pyroptosis. *Cell Res.* **25**, 1183–1184 (2015).
23. N. Kayagaki *et al.*, Caspase-11 cleaves gasdermin D for non-canonical inflammasome signaling. *Nature* **526**, 666–671 (2015).
24. J. Shi *et al.*, Cleavage of GSDMD by inflammatory caspases determines pyroptotic cell death. *Nature* **526**, 660–665 (2015).
25. X. Liu *et al.*, Inflammasome-activated gasdermin D causes pyroptosis by forming membrane pores. *Nature* **535**, 153–158 (2016).
26. K. S. G. de Sa *et al.*, Gasdermin-D activation promotes NLRP3 activation and host resistance to Leishmania infection. *Nat. Commun.* **14**, 1049 (2023).
27. J. F. Baum, L. Bredegaard, S. A. Herrera, T. G. Pomorski, Visualizing NBD-lipid Uptake in mammalian cells by confocal microscopy. *Bio. Protoc.* **13**, e4771 (2023).
28. K. Gulshan, G. Brubaker, S. Wang, S. L. Hazen, J. D. Smith, Sphingomyelin depletion impairs anionic phospholipid inward translocation and induces cholesterol efflux. *J. Biol. Chem.* **288**, 37166–37179 (2013).
29. M. T. Cheng *et al.*, Structural insights into the activation of autoinhibited human lipid flippase ATP8B1 upon substrate binding. *Proc. Natl. Acad. Sci. U.S.A.* **119**, e2118656119 (2022).
30. X. Zhou, T. R. Graham, Reconstitution of phospholipid translocase activity with purified Drs2p, a type-IV P-type ATPase from budding yeast. *Proc. Natl. Acad. Sci. U.S.A.* **106**, 16586–16591 (2009).
31. D. E. Hokanson, J. M. Laakso, T. Lin, D. Sept, E. M. Ostap, Myo1c binds phosphoinositides through a putative pleckstrin homology domain. *Mol. Biol. Cell* **17**, 4856–4865 (2006).
32. M. Mahajan *et al.*, NMR identification of a conserved Drp1 cardiolipin-binding motif essential for stress-induced mitochondrial fission. *Proc. Natl. Acad. Sci. U.S.A.* **118**, e2023079118 (2021).
33. A. C. Norris *et al.*, Deficiency of the lipid flippase ATP10A causes diet-induced dyslipidemia in female mice. *Sci Rep.* **14**, 343 (2024).
34. P. L. Schwartzberg, K. L. Mueller, H. Qi, J. L. Cannons, SLAM receptors and SAP influence lymphocyte interactions, development and function. *Nat. Rev. Immunol.* **9**, 39–46 (2009).
35. X. Wang, B. Yang, Y. Li, J. Luo, Y. Wang, AKR1C1 alleviates LPS-induced ALI in mice by activating the JAK2/STAT3 signaling pathway. *Mol. Med. Rep.* **24** (2021).
36. A. C. Doran, A. Yurdagul Jr., I. Tabas, Efferocytosis in health and disease. *Nat. Rev. Immunol.* **20**, 254–267 (2020).
37. Y. Kojima, I. L. Weissman, N. J. Leeper, The role of efferocytosis in atherosclerosis. *Circulation* **135**, 476–489 (2017).
38. L. Mu *et al.*, A phosphatidylinositol 4, 5-bisphosphate redistribution-based sensing mechanism initiates a phagocytosis program. *Nat. Commun.* **9**, 4259 (2018).
39. D. M. Schrijvers, G. R. De Meyer, M. M. Kockx, A. G. Herman, W. Martinet, Phagocytosis of apoptotic cells by macrophages is impaired in atherosclerosis. *Arterioscler. Thromb. Vasc. Biol.* **25**, 1256–1261 (2005).
40. S. Shah *et al.*, Strain background modifies phenotypes in the ATP8B1-deficient mouse. *PLoS One* **5**, e8984 (2010).
41. S. El-Kirat-Chatel, Y. F. Dufrene, Nanoscale adhesion forces between the fungal pathogen Candida albicans and macrophages. *Nanoscale Horiz.* **1**, 69–74 (2016).
42. N. R. Patel *et al.*, Cell elasticity determines macrophage function. *PLoS One* **7**, e41024 (2012).
43. Y. Zhao, G. Mahajan, C. R. Kothapalli, X. L. Sun, Sialylation status and mechanical properties of THP-1 macrophages upon LPS stimulation. *Biochem. Biophys. Res. Commun.* **518**, 573–578 (2019).
44. G. Bryant, J. Wolfe, Electromechanical stresses produced in the plasma membranes of suspended cells by applied electric fields. *J. Membr. Biol.* **96**, 129–139 (1987).
45. T. Dieudonne *et al.*, Autoinhibition and regulation by phosphoinositides of ATP8B1, a human lipid flippase associated with intrahepatic cholestatic disorders. *Elife* **11**, e75272 (2022).

46. I. Gerin *et al.*, Expression of miR-33 from an SREBP2 intron inhibits cholesterol export and fatty acid oxidation. *J. Biol. Chem.* **285**, 33652–33661 (2010).
47. T. J. Marquart, R. M. Allen, D. S. Ory, A. Baldan, miR-33 links SREBP-2 induction to repression of sterol transporters. *Proc. Natl. Acad. Sci. U.S.A.* **107**, 12228–12232 (2010).
48. K. J. Rayner *et al.*, MiR-33 contributes to the regulation of cholesterol homeostasis. *Science* **328**, 1570–1573 (2010).
49. S. H. Najafi-Shoushtari *et al.*, MicroRNA-33 and the SREBP host genes cooperate to control cholesterol homeostasis. *Science* **328**, 1566–1569 (2010).
50. R. M. Allen *et al.*, miR-33 controls the expression of biliary transporters, and mediates statin- and diet-induced hepatotoxicity. *EMBO Mol. Med.* **4**, 882–895 (2012).
51. W. L. van der Woerd *et al.*, Mutational analysis of ATP8B1 in patients with chronic pancreatitis. *PLoS One* **8**, e80553 (2013).
52. A. Mehl, H. Bohorquez, M. S. Serrano, G. Galliano, T. W. Reichman, Liver transplantation and the management of progressive familial intrahepatic cholestasis in children. *World J. Transplant.* **6**, 278–290 (2016).
53. H. Wang *et al.*, ORP2 delivers cholesterol to the plasma membrane in exchange for phosphatidylinositol 4, 5-bisphosphate ($PI(_{4,5})P_2$). *Mol Cell* **73**, 458–473.e7 (2019).
54. R. Ghai *et al.*, ORP5 and ORP8 bind phosphatidylinositol-4, 5-bisphosphate (PtdIns(4, 5)P_2) and regulate its level at the plasma membrane. *Nat. Commun.* **8**, 757 (2017).
55. C. Settembre *et al.*, TFEB links autophagy to lysosomal biogenesis. *Science* **332**, 1429–1433 (2011).
56. R. David, Autophagy: TFEB perfects multitasking. *Nat. Rev. Mol. Cell Biol.* **12**, 404 (2011).
57. H. Hayashi *et al.*, Assessment of ATP8B1 deficiency in pediatric patients with cholestasis using peripheral blood monocyte-derived macrophages. *EBioMedicine* **27**, 187–199 (2018).
58. V. A. van der Mark *et al.*, Phospholipid flippases attenuate LPS-induced TLR4 signaling by mediating endocytic retrieval of Toll-like receptor 4. *Cell. Mol. Life Sci.* **74**, 715–730 (2017).
59. P. J. Koelink *et al.*, The phospholipid flippase ATP8B1 is involved in the pathogenesis of ulcerative colitis via establishment of intestinal barrier function. *J. Crohn. Colitis* **18**, 1134–1146 (2024).
60. S. Leporatti *et al.*, Elasticity and adhesion of resting and lipopolysaccharide-stimulated macrophages. *FEBS Lett.* **580**, 450–454 (2006).
61. A. J. Iacano *et al.*, Miltefosine increases macrophage cholesterol release and inhibits NLRP3-inflammasome assembly and IL-1β release. *Sci. Rep.* **9**, 11128 (2019).
62. N. Guz, M. Dokukin, V. Kalaparthi, I. Sokolov, If cell mechanics can be described by elastic modulus: Study of different models and probes used in indentation experiments. *Biophys. J.* **107**, 564–575 (2014).